




Article

Multi-Objective Grasshopper Optimization Based MPPT and VSC Control of Grid-Tied PV-Battery System

Mukul Chankaya ¹, Ikhlq Hussain ², Aijaz Ahmad ¹, Hasmat Malik ^{3,*} and Fausto Pedro García Márquez ⁴

¹ Department of Electrical Engineering, NIT Srinagar, Srinagar 190006, India; mukulchankaya@gmail.com (M.C.); aijaz54@nitsri.net (A.A.)

² Department of Electrical Engineering, University of Kashmir, Srinagar 190006, India; ikhlaqjtd2015@gmail.com

³ BEARS, NUS Campus, University Town, Singapore 138602, Singapore

⁴ Ingenium Research Group, Universidad Castilla-La Mancha, 13071 Ciudad Real, Spain; faustopedro.garcia@uclm.es

* Correspondence: hasmat.malik@gmail.com

Abstract: This article presents the control of a three-phase three-wire (3P-3W) dual-stage grid-tied PV-battery storage system using a multi-objective grass-hopper optimization (MOGHO) algorithm. The voltage source converter (VSC) control of the presented system is implemented with adaptive kernel width sixth-order maximum correntropy criteria (AKWSOMCC) and maximum power point tracking (MPPT) control is accomplished using the variable step-size incremental conductance (VSS-InC) technique. The proposed VSC control offers lower mean square error and better accuracy, convergence rate and speed as compared to peer adaptive algorithms, i.e., least mean square (LMS), least mean fourth (LMF), maximum correntropy criteria (MCC), etc. The adaptive Gaussian kernel width is a function of the error signal, which changes to accommodate and filter Gaussian and non-Gaussian noise signals in each iteration. The VSS-InC based MPPT is provided with a MOGHO based modulation factor for better and faster tracking of the maximum power point during changing solar irradiation. Similarly, an optimized gain conventional PI controller regulates the DC bus to improve the power quality, and DC link stability during dynamic conditions. The optimized DC-link generates an accurate loss component of current, which further improves the VSC capability of fundamental load current component extraction. The VSC is designed to perform multi-functional operations, i.e., harmonics elimination, reactive power compensation, load balancing and power balancing at point of common coupling during diverse dynamic conditions. The MOSHO based VSS-InC, and DC bus performance is compared to particle swarm optimization (PSO) and genetic algorithm (GA). The proposed system operates satisfactorily as per IEEE519 standards in the MATLAB simulation environment.

Keywords: adaptive control; battery storage; MPPT; power electronics; power quality; photovoltaic; optimization



Citation: Chankaya, M.; Hussain, I.; Ahmad, A.; Malik, H.; García Márquez, F.P. Multi-Objective Grasshopper Optimization Based MPPT and VSC Control of Grid-Tied PV-Battery System. *Electronics* **2021**, *10*, 2770. <https://doi.org/10.3390/electronics10222770>

Academic Editors: Hamid Reza Karimi, Valeri Mladenov, Kalyana C. Veluvolu, Len Gelman, Jun Yang, Cecilio Angulo, Cheng Siong Chin and Davide Astolfi

Received: 18 September 2021

Accepted: 9 November 2021

Published: 12 November 2021

Publisher's Note: MDPI stays neutral with regard to jurisdictional claims in published maps and institutional affiliations.



Copyright: © 2021 by the authors. Licensee MDPI, Basel, Switzerland. This article is an open access article distributed under the terms and conditions of the Creative Commons Attribution (CC BY) license (<https://creativecommons.org/licenses/by/4.0/>).

1. Introduction

The grid-tied Photovoltaic (PV) system has become a natural choice for green energy, considering PV power's sharp cost curtailment [1]. The grid-tied PV systems have shown considerable commitment as a stable and reliable participant in the modern power grid [2,3].

Maximum power point tracking (MPPT) is crucial for achieving the desired efficiency and payback time of PV systems [4]. In [5,6], a detailed review of widely used traditional, intelligent and optimization based MPPT methods have been provided. In [7], an exhaustive review of artificial neural network (ANN) based MPPT has been provided along with ANN-based variable step-size MPPT is also proposed. The perturb and observe (P&O) and incremental conductance (InC) based MPPTs are among the widely implemented techniques due to their ease of implementation, reduced computational burden and adequate

efficiency. In conventional InC and P&O techniques, the step size or duty cycle perturbation (ΔD) remains fixed, where the trade-off has to be made between faster response and oscillations across the maximum power point (MPP). During steady-state smaller ΔD is desirable, which reduces the operating point oscillations across MPP and eventually PV power (P_{PV}) oscillations. Whereas, during a dynamic state larger ΔD contributes to the faster dynamics and helps in the quick attainment of the MPP [8].

The variable step-size P&O/InC MPPT offers the extra advantage of easy implementation and lower computational burden, can be implemented by various methods, where most of the algorithms are very similar, i.e., ΔD changed according to the multiplication of modulation or scaling factor (δ) and derivative of power to current ($\delta * \Delta P / \Delta I$) [9], or to voltage ($\delta * \Delta P / \Delta V$) [10] or to step-change in duty cycle ($\delta * \Delta P / \Delta D$) [11]. In [9] variable step-size InC (VSS-InC) MPPT is implemented for the boost control, which shows good dynamic response but suffers from high overshoot due to fixed δ . In [10] according to the experimental observation, VSS-InC/P&O MPPT controls the boost converter, where δ is kept between 1 to 2.5% of the inverse of PV current (I_{PV}^{-1}). In [11] δ is autotuned for the robust performance of buck converter control by VSS-P&O MPPT at the cost of the computational burden. In [12], load current based adaptive step size MPPT is suggested, D is made a function of derivative of current to change in duty cycle ($\Delta I / \Delta D$) where δ is kept constant. In [13], for the VSS-InC method, $\delta = 0.001$ is chosen at the design stage and ΔD is made a function of the power derivative on the difference of voltage and current derivatives ($\delta * \Delta P / (\Delta V - \Delta I)$). The selection of δ is crucial for the MPPT performance and bad selection may introduce steady-state oscillations and slow down the tracking speed. In [14] the $\delta < \Delta D_{max} / |dP/dV|$ is suggested to improve the performance of VSS-InC MPPT. In [15], a modified P&O method utilizes a direct duty ratio control for achieving drift-free MPPT operation at the first step-change in duty cycle during rapidly changing irradiation levels. The InC—with self-adaptive and immanent decision-making capability—is presented in [16], where three consecutive points on the power-voltage curve accurately detect the steady and dynamic conditions. In the presented work, the δ has been optimized for the VSS-InC MPPT as the first objective of the implemented multi-objective grasshopper optimization (MOGHO) algorithm [17]. The designing of δ is performed on an offline basis, it does not affect the computational complexity of the VSS-InC, improves the MPP tracking speed and accuracy.

The DC bus is of utmost importance for the stability of the system. The DC link voltage (V_{dc}) is regulated by the conventional PI controller. Meta-heuristic optimization techniques (MOT) have been frequently used for PI controller gain optimization, which reduces the V_{dc} transients during a steady and dynamic state and increase the DC link stability [18]. In [19] the Jaya algorithm is employed to increase the power quality by optimizing the PI controller gains and filter parameters. The Jaya algorithm is a specific parameter less technique that is robust but less efficient. In [20,21], the DC link optimization with the salp swarm optimization (SSO) technique and generalized normal distributed algorithm (GNDO) are presented. The SSO technique delivers a poor convergence rate on higher-dimensional problems and GNDO is inspired by the Gaussian distribution and require no special controlling parameters. In [22], the comparative analysis of regulated V_{dc} with whale optimization algorithm (WOA) and particle swarm optimization (PSO) is performed. Both WOA and PSO suffers from slow convergence, low accuracy, and local minima stagnation. Many potent deep reinforcement learning (DRL) based optimization techniques, i.e., soft actor-critic (SAC) [23], deep deterministic policy gradient (DDPG) [24], expert assistant DDPG (EADDPG) techniques [25], etc. can further be utilized for the performance enhancement of grid-tied PV systems. In the presented work, MOGHO is utilized for the V_{dc} regulation by PI controller gains optimization as the second objective of multi-objective optimization techniques. The MOGHO offers a better convergence rate and balance between the exploration and exploitation phase which ensures to reduce the chances of local minima stagnation [17].

Numerous VSC control algorithms of various domains such as time domain, frequency domain, adaptive controls etc. for the grid-tied PV system have been investigated and implemented by the researchers. The synchronous reference frame (SRF), power balance theory (PBT), and many more [26] are among the widely used time-domain techniques, which are easy to implement and have less computational burden but produce more steady-state error. In [27], active reactive power control of instantaneous and average nature (IARC and AARC), balanced positive sequence compensation (BPSC), positive-negative sequence compensation (PNSC), etc. based on VSC controls have been proposed. The frequency-domain controls, i.e., Kalman filter-based controls (KFC) [28], Stockwell transformation (ST), etc. [29] have higher computational complexity and slow convergence speed. On the other hand, adaptive controls have a moderate computational burden and deliver reduced steady-state error with a faster convergence speed. Adaptive algorithms such as least mean square (LMS) [30], least mean fourth (LMF) [31], maximum correntropy criteria (MCC) [32] deliver faster convergence and robustness. The LMS control due to the fixed step size, produce a relatively higher steady-state error as compared to the LMF, which acts as a higher-order filter for the error signal. The MCC utilizes the Gaussian kernel which is effective against both Gaussian and non-Gaussian noise signals. Many advanced versions of LMS, LMF and MCC, i.e., hyperbolic cosine LMS (HCLMS) [33], hyperbolic tangent function (HTF) [34], LMS-LMF [35], adaptive neuro-fuzzy LMS (ANF-LMS) [36], zero attracting normalized LMF (ZAN-LMF) [37], normalized MCC (NMCC) [38], fixed forward prediction (FFP) [39], adaptive kernel width sixth-order MCC (AKWSOMCC) [40], etc. The HC-LMS offers minimal dynamic oscillations, HTF acts as a higher-order filter, which offers reduced mean square error (MSE), combined LMS-LMF reduces the shortcomings of LMS control by switching between second and fourth-order filter, but the performance of both controls reduces during heavily tailed Gaussian noises due to fixed step-size. The ANF-LMS delivers neuro-fuzzy tuned step-size for enhanced performance but increases the computational complexity. The ZAN-LMF, NMCC and FPP vouch for faster convergence rate and speed but have a high steady-state error due to fixed step size. The AKWSOMCC can handle Gaussian and non-Gaussian noises efficiently, while acting as a higher-order filter and delivering a better fundamental load current component. The function approximation and noise cancellation offered by AKWSOMCC are better than its peer adaptive controls due to adaptive kernel width, which also improves the convergence speed despite computational complexity. The proposed AKWSOMCC algorithms parameters are carefully tuned depending on their application ensuring the desired performance during the diverse dynamic condition. The optimized MPPT and DC bus further enhance the capability of the proposed control.

In the presented work, the MOGHO algorithm fulfils two objectives by providing the optimum δ for VSS-InC MPPT and PI controller gains (k_p, k_i) for the V_{dc} control, in a three-phase three-wire (3P-3W) grid-tied dual-stage PV-battery storage system. The VSC is controlled by the AKWSOMCC algorithm. During steady-state and dynamic states, the VSC control performs harmonics suppression, reactive power compensation, load balancing and active power balancing at the point of common coupling (PCC). The battery storage system maintains the power balance during dynamic conditions. The optimized DC bus generates an accurate loss current component, which further enhances the system's performance. The main attributes of the proposed work are as follows:

- a. MOGHO based scaling factor (δ) optimization for VSS-InC MPPT to achieve faster tracking and reduced power oscillations at MPP.
- b. MOGHO based PI controller gains (k_p, k_i) optimization for the V_{dc} control and generation of an accurate loss current component (i_{Loss}).
- c. AKWSOMCC based VSC control for fundamental load current component extraction.

2. System Description

The proposed topology is presented in Figure 1. A dual-stage PV system of 33 kW along with battery storage is integrated with the 3P-3W grid. The PV array and battery design parameters are provided in Appendix A. The MOGHO algorithm optimizes the δ of VSS-InC based MPPT and PI controller gains (k_p & k_i) for V_{dc} regulation. The boost converter is controlled by the gating signal delivered by the MPPT to stabilize the V_{PV} . The battery current control during the charging and discharging phase is aided by the bi-directional buck-boost converter. The coupling capacitor at the DC link connects the DC and AC systems. The 3P-3W converter is attached to the PCC through interfacing inductors and ripple filters. The non-linear load of 16.5 kW and distribution grid of 415 V at 50 Hz are also attached to PCC.

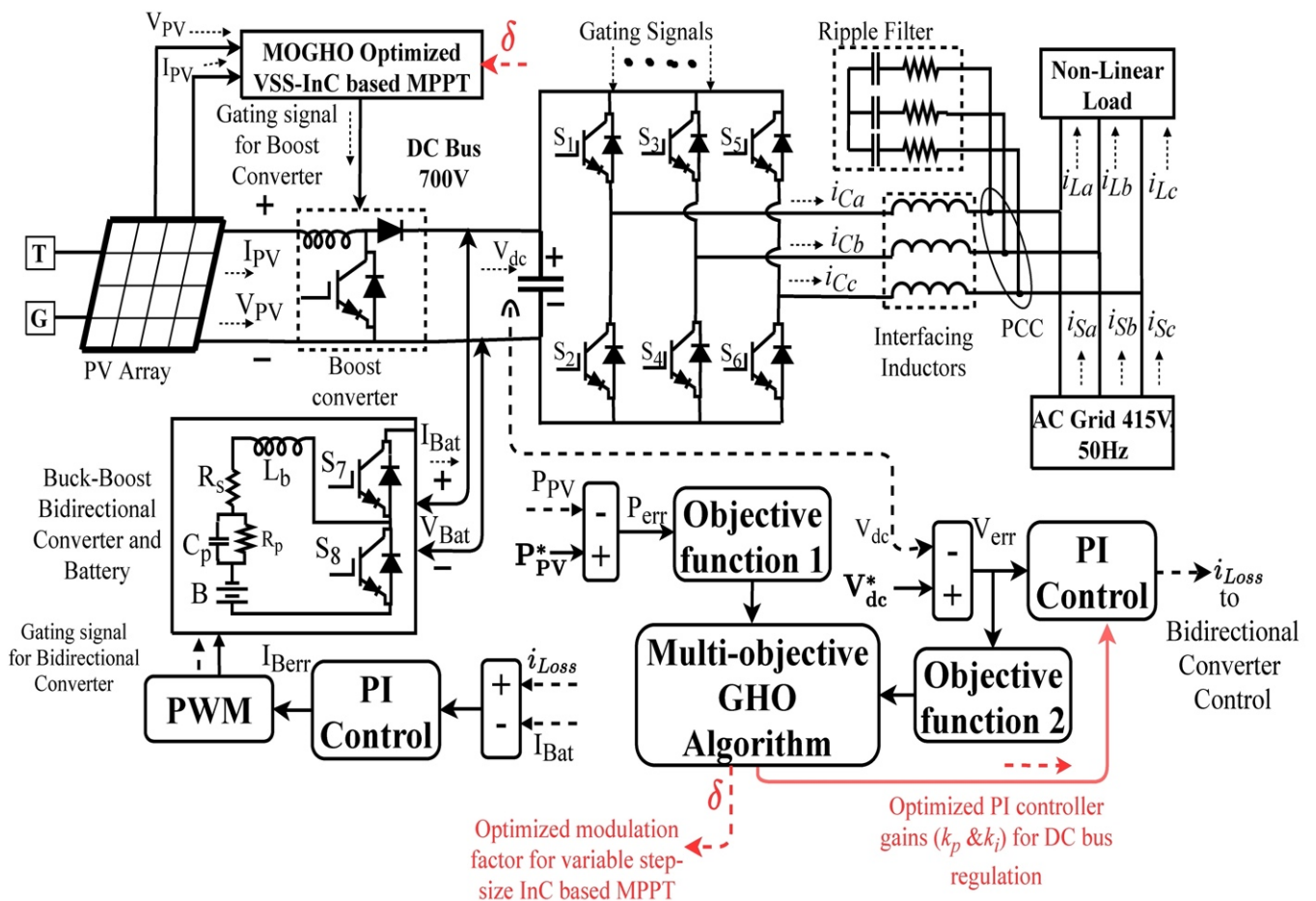


Figure 1. Proposed topology.

3. Implemented Research Methodology

The implemented research methodology is depicted in Figure 2. The V_{PV} , I_{PV} , V_{dc} , grid voltage magnitude (V_t), source voltage (v_{Sabc}) and current (i_{Sabc}) are sensed from the simulated system. The derivative of PV power (P_{PV}) from the reference value (P_{PV}^*) is utilized for the generation of first integral square error (ISE-1) as the first objective function (Obj-1) to be minimized by the MOGHO algorithm as per (1). The optimized VSS-InC MPPT regulates the boost converter. At the DC bus, the comparison of V_{dc} and (V_{dc}^*) is formed into second integral square error (ISE-2) as the second objective function (Obj-2) for MOGHO algorithm as per (2). The ISE as error indices is chosen, considering the decaying error with time. The MOGHO algorithm delivers the optimized δ and k_p & k_i for the DC

bus control. The accurate i_{Loss} current and feed-forward term (W_{PV}) are provided to the AKWSOMCC for generating the switching signals of VSC control.

$$\text{Obj-1} = \int_0^t (P_{PV}^* - P_{PV}) = \int_0^t P_{err}^2 \quad (1)$$

$$\text{Obj-2} = \int_0^t (V_{dc}^* - V_{dc}) = \int_0^t V_{err}^2 \quad (2)$$

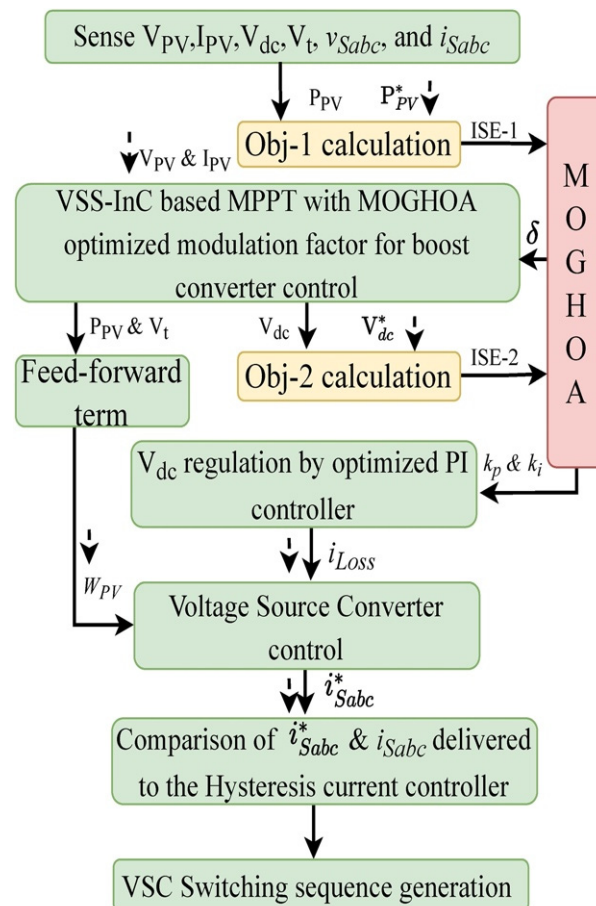


Figure 2. Research methodology.

4. Multi-Objective Grass-Hopper Optimization Algorithm and Implementation

The MOGHO is a nature-inspired swarm intelligence (SI) technique that is based on the natural foraging and swarming behaviour of the grasshoppers. The grasshopper life cycle in two phases, i.e., nymph and adult are considered, where nymph does not have wings and move in the wind direction, whereas adults have wings and can travel a larger distance. The flow chart of the MOGHO is shown in Figure 3.

The grasshopper swarm is mathematically represented as (3), where P_i is the fitness function, S_i is the social interaction term, G_i is the gravity term, A_i is the wind advection term. The r_1 , r_2 , and r_3 are the random numbers within $[0, 1]$, which introduces randomness.

$$P_i = r_1 S_i + r_2 G_i + r_3 A_i \quad (3)$$

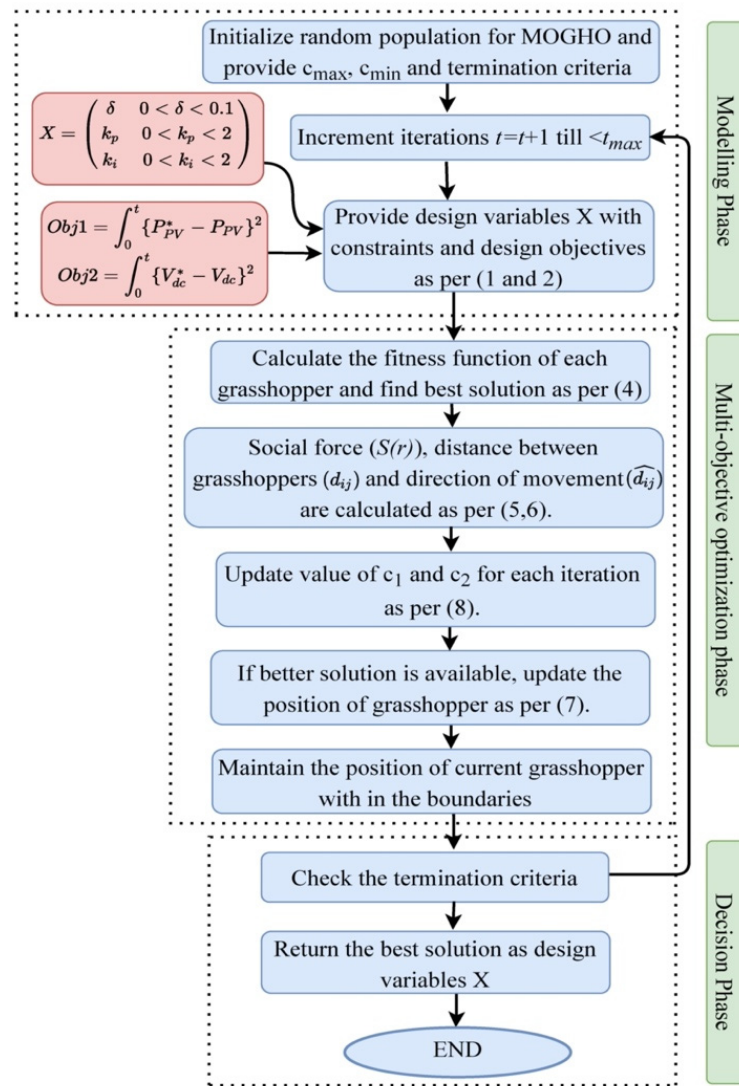


Figure 3. MOGHO flowchart.

The complete equation of the MOGHO is presented as per (4).

$$P_i = r_1 \underbrace{\left[\sum_{\substack{j=1 \\ j \neq i}}^N S(r) * (d_{ij}) \hat{d}_{ij} \right]}_{S_i} + r_2 \underbrace{(-g\hat{e}_g)}_{G_i} + r_3 \underbrace{(u\hat{e}_w)}_{A_i} \tag{4}$$

The social interaction of grasshoppers is highly dependent on their social force and the distance between them. The social force $S(r)$ is calculated as per (5), where f is the attraction intensity and l is the attractive length scale. The $S(r)$ governs the social attraction and repulsion (or exploitation and exploration) of the grasshoppers. If f and l vary in the interval $[0, 2.079]$ repulsion will occur and if f and l vary in the interval $[2.079, 4]$ attraction will happen in grasshoppers. The grasshopper will be in its comfort zone when f and l remain exactly at 2.079. The d_{ij} is the distance between i^{th} and j^{th} grasshopper and \hat{d}_{ij} is a unit vector showing the direction of the grasshopper movement.

$$S(r) = fexp(-\frac{r}{l_b}) - exp(-r) \tag{5}$$

$$d_{ij} = |P_j - P_i|; \hat{d}_{ij} = \frac{P_j - P_i}{d_{ij}} \tag{6}$$

The G_i depending on gravitational constant (g) and unit vector \hat{e}_g towards the centre of the earth. The A_i term is a function of a constant u and unit vector \hat{e}_w in wind direction. The grasshopper swarm behaviour of reaching and staying in the comfort zone can lead the iterative process towards local minima stagnation. For better chances of convergence, the modified equation of MOGHO is utilized as per (7).

$$P_i = r_1 c_1 \left(\sum_{\substack{j=1 \\ j \neq i}}^N c_2 \left(\frac{u_b - l_b}{2} \right) S(r) * (d_{ij}) \hat{d}_{ij} \right) + \hat{T}_d \tag{7}$$

$$c = c_1 = c_2 = c_{max} - t \left(\frac{c_{max} - c_{min}}{t_{max}} \right) \tag{8}$$

The comfort zone coefficient ($c = c_1 = c_2$) calculated as per (8) will have the same value but a different impact on the fitness function calculation as per (7). The c_1 is similar to the inertial weight in PSO, which reduces the search area as the iterations increases to balance the exploration and exploitation phase. The c_2 term reduces the repulsion, comfort, and repulsion zone (or the search area around global optima) between grasshoppers linearly to increase the chances of convergence and reduce the local minima stagnation. c_{max} and c_{min} are chosen as 1 and 0.000001 for the current problem. At the end of the iterative process, the MOGHO delivers the optimized δ and k_p, k_i gains. The presented system is aided with the four dedicated controls, i.e., optimized VSS-InC based MPPT control, bi-directional converter control, optimized V_{dc} control and AKWSOMCC based VSC control.

4.1. MOGHO Based VSS-InC MPPT Control

The flow chart for the MOGHO based VSS-InC MPPT is shown in Figure 4. The VSS-InC varies the D with ΔD as perturbation step instead of fixed perturbation in conventional InC algorithm. The MPP is achieved when the variance of output conductance equals the negative of output conductance or the slope of the power-voltage ($P-V$) curve reaches zero as in the conventional InC algorithm as per (10).

$$\Delta D = D(n) - D(n - 1) = D_{min} + \delta * \left(\frac{P(n) - P(n - 1)}{V(n) - V(n - 1)} \right) \tag{9}$$

$$\frac{\Delta I_{PV}}{\Delta V_{PV}} = - \frac{I_{PV}}{V_{PV}} \text{ At MPP} \tag{10}$$

The upper and lower bounds for δ optimization are selected based on experimental data presented in [7], which is 1–2.5% of I_{PV}^{-1} and likewise the D_{min} is also selected. The δ optimization is performed offline to reduce the computational burden of MPPT and optimized VSS-InC MPPT offers better efficiency, faster MPP tracking and reduced steady-state oscillations as compared to conventional InC MPPT algorithm. The variable and fixed step size MPPT operation are described in Figure 5. With a larger fixed step size, the MPP tracking will be very fast but chances of oscillations across MPP will be very high during steady-state, which gets reflected in higher P_{PV} oscillations. The smaller fixed step size increases the efficiency and reduces the steady-state oscillations, but the tracking speed reduces. The variable step size uses a larger step size during irradiation change to reach quickly near the MPP and gradually reduces the step size near MPP to avoid the oscillations.

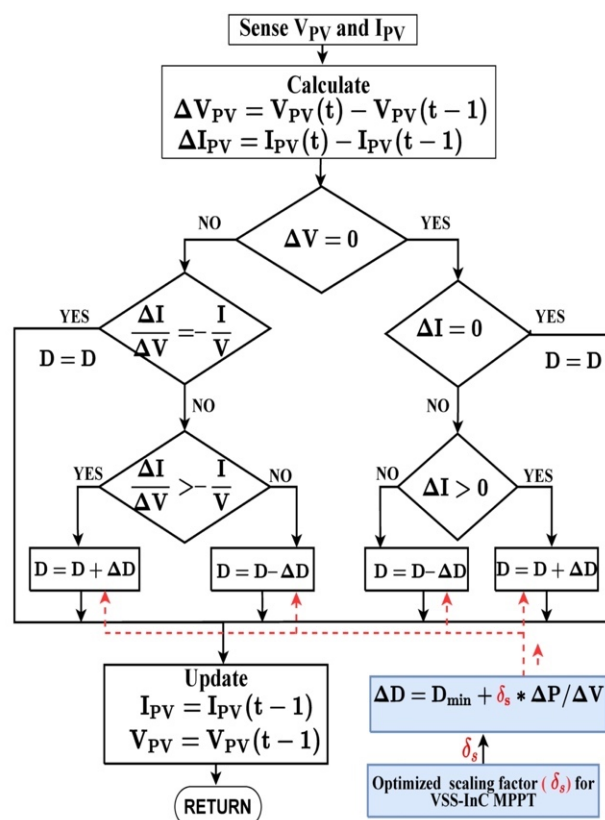


Figure 4. MOGHO algorithm based VSS-InC MPPT.

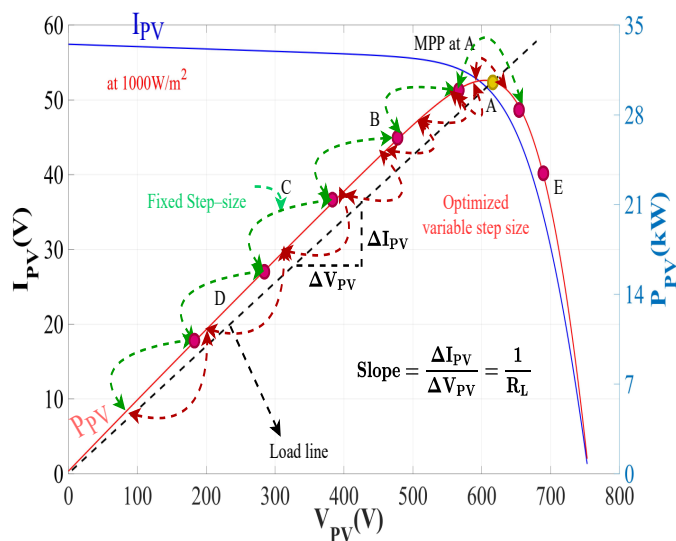


Figure 5. Variable and fixed step size MPPT operation.

4.2. MOGHO Based V_{dc} Control

The battery current control and V_{dc} control is shown in Figure 6. The DC bus is regulated by a conventional PI controller, which is tuned with the MOGHO algorithm. The MOGHO algorithm minimizes the Obj-2 and delivers the optimized gains for better stabilization of the V_{dc} and generation of an accurate i_{Loss} current during dynamic conditions [13].

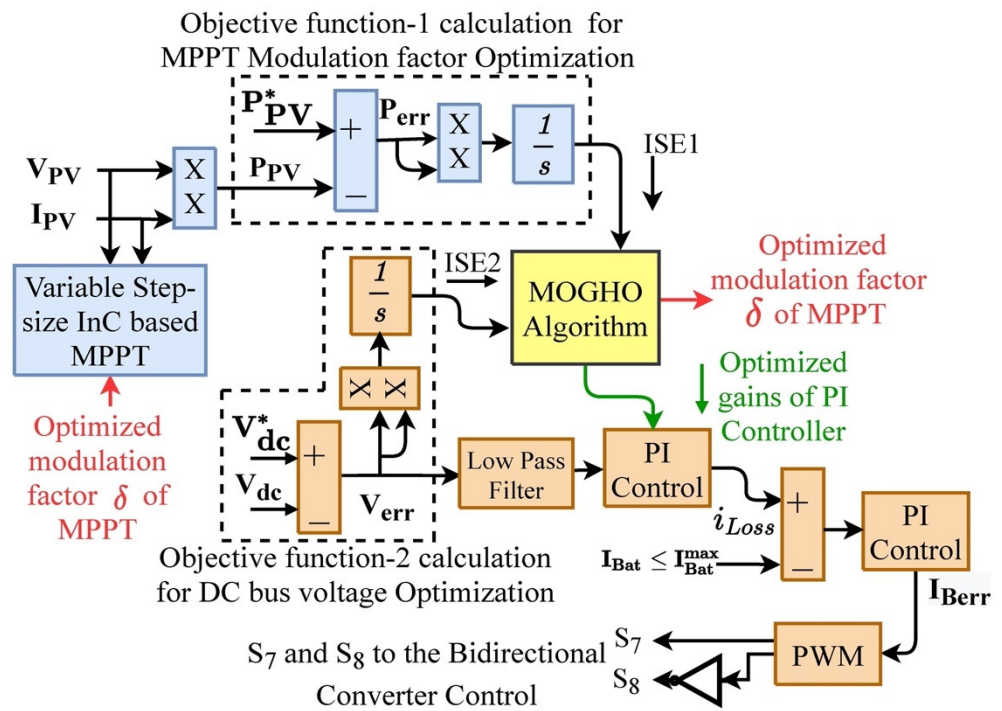


Figure 6. Bi-directional converter and DC bus voltage control.

The comparison of i_{Loss} and battery current (I_{Bat}) is fed to another PI controller, by which pulse width modulator (PWM) with logic gate, generates the adequate switching sequence. For the battery overcurrent protection, the I_{Bat} is limited during charging and discharging up to $I_{Bat}^{max} = 30$ A. The I_{Bat} control during the charging and discharging stage is performed by S_7 and S_8 switches of the bi-directional buck-boost converter.

5. AKWSOMCC Based VSC Control

The AKWSOMCC based compensator control is implemented by varying the kernel width as a function of the error signal as shown in Figure 7. The proper selection of the kernel width results in the smoothness of function approximation, better convergence rate and accuracy. The larger the kernel width, function smoothness will be more, but reduces sensitivity and may only behave as LMS. With a smaller kernel width, the locality of the training data is preserved, but the convergence rate will slow down. The proposed control with adaptive width brings the Gaussian and non-Gaussian noises of the error signal in the “observation window”. The adaptive Gaussian kernel width is a function of error signals, try to cover all Gaussian and non-Gaussian noises under the Gaussian bell curve for filtration. With adaptive kernel width, the whole network matrix or observation window need not be analysed, hence convergence speed increases. The sixth-order MCC acts as a higher-order adaptive filter with sixth-order power optimization. The MSE reduction with higher-order filters produces better steady-state behaviour. The adaptive kernel width (σ_n) is a function of the error signal and fixed kernel width (σ_0) as per (11). The pre-decided kernel width ($\sigma_0 = 10$) will remain fixed during operation [27]. The error signal (e_{nx}) is generated as per (12).

$$\sigma_n^2 = e_{nx}^2 + \sigma_0^2; \text{ where } x = (a, b, c) \tag{11}$$

$$e_{nx} = i_{La} - \mu_{pa} * W_{sp}; \text{ where } x = (a, b, c) \tag{12}$$

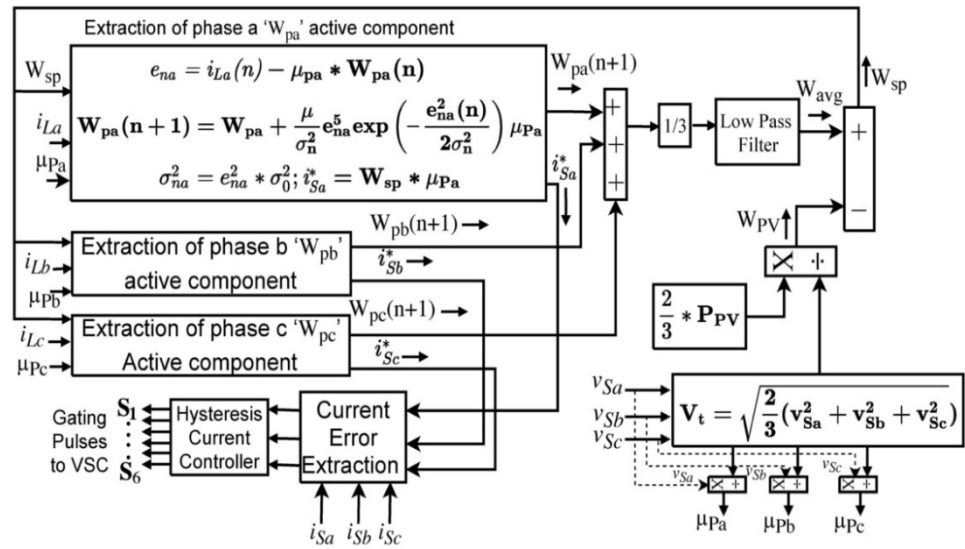


Figure 7. AKWSOMCC based VSC control.

The weight signals of each phase $W_{pa}(n + 1)$, $W_{pb}(n + 1)$ and $W_{pc}(n + 1)$ are generated as per (13).

$$W_{px}(n + 1) = W_{px}(n) + e_{nx}^5 \frac{\mu * \mu_{px}}{\sigma_n^2} \exp\left(-\frac{e_{nx}^2}{2(\sigma_n^2)}\right) \text{ where } x = (a, b, c) \quad (13)$$

The μ is the step size, $\mu_{pa}, \mu_{pb}, \mu_{pc}$ are the unit templates or the in-phase components of source voltage generated as $\mu_{pa} = v_{Sx}/V_t$ (where $x = a, b, c$), where V_t is the voltage magnitude and v_{Sx} will be the phase to ground source voltage. The W_{avg} is the average weight signal calculated as per (14). The feed-forward term (W_{PV}) is introduced in the VSC control for the power balancing is calculated as per (15), where V_{PV} and I_{PV} are the PV voltage and current signal.

$$W_{avg} = \frac{1}{3} (W_{pa} + W_{pb} + W_{pc}) \quad (14)$$

$$W_{PV} = \frac{2}{3} \left(\frac{V_{PV} * I_{PV}}{V_t} \right); \text{ where } V_t = \sqrt{\frac{2}{3} (v_{Sa}^2 + v_{Sb}^2 + v_{Sc}^2)} \quad (15)$$

The W_{sp} will be the overall weight generated as per (16), which is further utilized for the current reference generation (i_{sx}^* ; where $x = a, b, c$) as per (17). During specified power mode, the $W_{sp_{fix}}$ will replace the W_{sp} as per (18) and generate the reference currents ($i_{sx_{fix}}^*$) as per (19).

$$W_{sp} = W_{avg} - W_{pv} \quad (16)$$

$$i_{sx}^* = W_{sp} * \mu_{px}; \text{ where } x = (a, b, c) \quad (17)$$

$$W_{sp_{fix}} = \frac{2}{3} \left(\frac{P_{fix}}{V_t} \right) \quad (18)$$

$$i_{sx_{fix}}^* = W_{sp_{fix}} * \mu_{px}; \text{ where } x = (a, b, c) \quad (19)$$

6. Results and Discussion

The system is scrutinized under steady-state, irradiation variation mode, specified power mode, unbalanced grid voltage, abnormal grid voltage, unbalanced load, islanding, and re-synchronization mode, with optimized Duty cycle and V_{dc} .

6.1. MOGHO Based VSS-InC MPPT Analysis

The V_{PV} performance with MOGHO, PSO, and GA optimized δ for VSS-InC MPPT is compared to the non-optimized or initially selected fixed δ VSS-InC MPPT presented in Figure 8a. The non-optimized fixed δ is selected as 0.0001. During the steady-state at irradiation level of 1000 W/m^2 the V_{PV} variations are minimum with MOGHO tuned MPPT, whereas with fixed δ VSS-InC variations are significant and continuous. The PSO and GA optimized MPPT also reduce the V_{PV} steady-state variations and performed comparatively better than non-optimized MPPT. During irradiation change from 1000 W/m^2 to 600 W/m^2 and vice versa, the MOGHO tuned MPPT manages to track MPP more quickly and accurately to settle down to the reference V_{PV} .

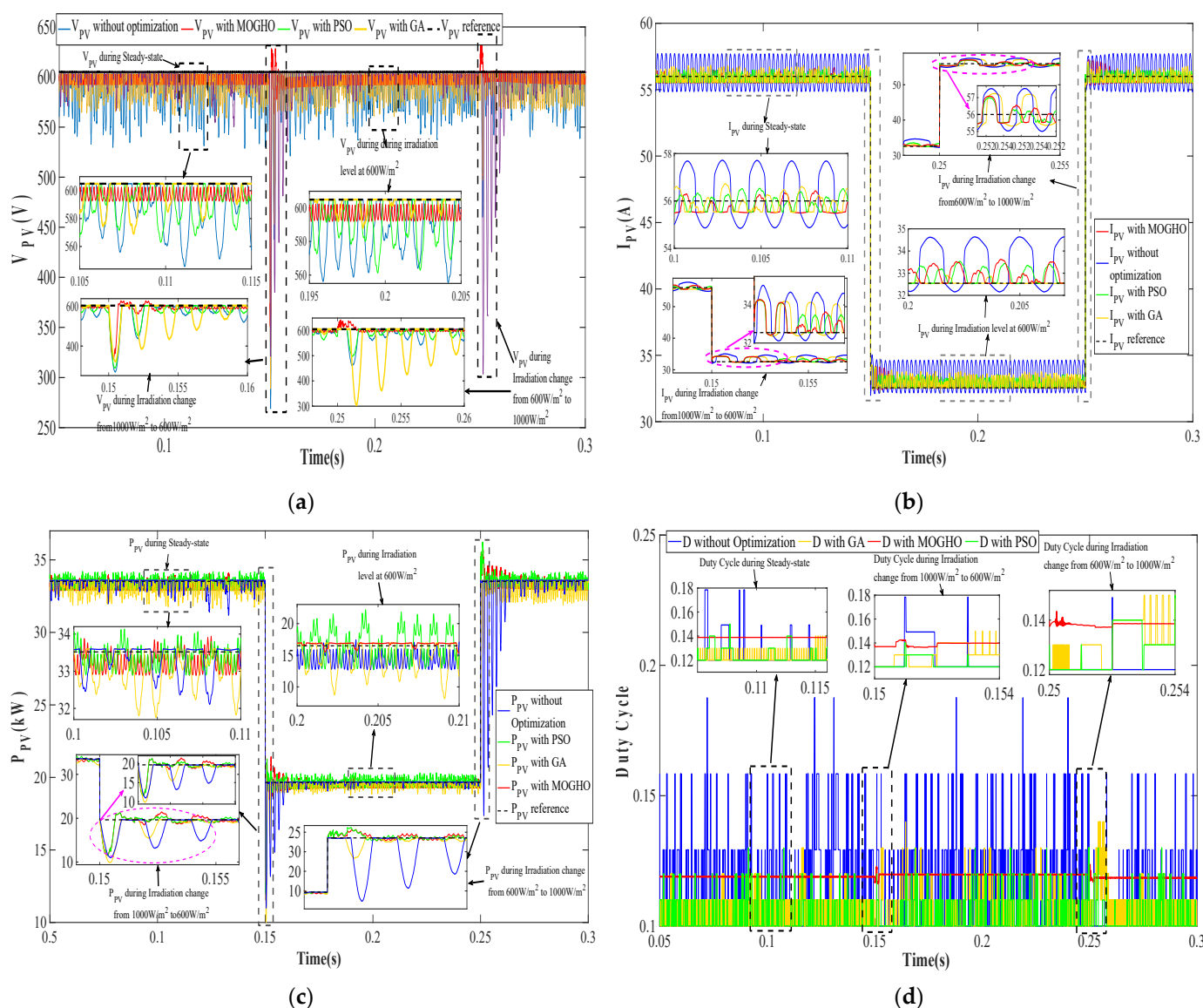


Figure 8. (a–d) System performance with optimized δ VSS-InC during steady-state and irradiation variation of (a) V_{PV} (b) I_{PV} (c) P_{PV} (d) D.

The I_{PV} comparison with MOGHO, PSO, GA optimized VSS-InC MPPT is compared with non-optimized VSS-InC MPPT in Figure 8b. During steady-state, MOGHO tuned MPPT maintains the I_{PV} close to its reference value, while performing better than PSO and GA tuned MPPT. Even during irradiation variations, the I_{PV} variations with MOGHO tuned MPPT remain minimum, which dies out more quickly due to faster and accurate tracking of MPP.

The P_{PV} also performs better with MOGHO tuned VSS-InC MPPT in comparison with PSO and GA techniques as shown in Figure 8c. The P_{PV} with adequate step size closely tracks P_{PV} and deliver more average power, hence improving the MPPT efficiency. During irradiation variations, P_{PV} variations are significantly reduced due to the accurate MPP tracking with MOGHO tuned VSS-InC MPPT.

The duty cycle (D) generated by the MOGHO tuned VSS-InC MPPT kept around the desired value, i.e., $D = 0.137$ as shown in Figure 8d. The D with MOGHO algorithm accurately tracks the MPP and takes very small steps to avoid the chances of oscillations around MPP. During dynamic state, the steps size increases to operate on a new load line and quickly track the shifted MPP for maximum power extraction. The D generated by MOGHO tuned MPPT during changing irradiances reduces the power oscillations to a greater extent and enhances the boost converter efficiency. Table 1 shows the comparative analysis of V_{PV} , I_{PV} settling time and boost converter efficiency with MOGHO, GA, PSO tuned MPPT and non-optimized VSS-InC MPPT with fixed δ . The VSC efficiency with MOGHO, GA, PSO tuned DC bus and non-optimized DC bus along with total dual-stage PV losses are also presented in Table 1.

Table 1. MPPT, boost converter and VSC performance analysis during sudden irradiation level change.

Parameters	MOGHO	PSO	GA	With Initially Selected δ
V_{PV} settling time	2.11 ms	3.04 ms	3.75 ms	12.50 ms
I_{PV} settling time	2.12 ms	3.02 ms	3.74 ms	13.25 ms
Boost Converter Efficiency	99.82%	99.61%	99.42%	98.82%
VSC Efficiency	99.23%	99.11%	98.79%	98.47%
Total dual-stage Losses (W)	308 W	414 W	580 W	875 W

6.2. MOGHO Algorithm Based DC Bus Analysis

The V_{dc} is regulated by the MOGHO tuned conventional PI controller. The V_{dc} should be maintained close to its reference value (V_{dc}^*) to ensure the stability of the system throughout the steady and dynamic states. The MOGHO regulated V_{dc} remains close to V_{dc}^* with minimum variations as compared to PSO regulated, GA regulated and non-optimized DC bus (with initially selected gains) during diverse dynamic conditions, i.e., initial transients, irradiation variation, unbalanced load, specified power mode and abnormal grid voltage as shown in Figure 9a. The optimized DC bus generates an accurate loss component of current which is further utilized in battery current control (I_{Bat}) as shown in Figure 6. The i_{Loss} current is shown in Figure 9b, where the MOGHO based i_{Loss} current have minimum variation as compared to PSO and GA. The MOGHO based accurate i_{Loss} current reduces the I_{Bat} ripples and improves the overall performance of bi-directional converter control. Table 2 presents the optimized design variables, i.e., k_p , k_i and δ with various optimization techniques and their initially selected or non-optimized values. The initially chosen or non-optimized design variables also serves as the initial condition for the implemented optimization techniques. Table 3 shows the comparative performance of V_{dc} during diverse dynamic conditions with MOGHO, PSO and GA optimization techniques.

Table 2. Optimized design variables (k_p , k_i and δ).

Decision Variables	MOGHO	PSO	GA	Without Optimization
k_p	1.22	0.94	0.82	1
k_i	0.89	0.71	0.38	0
δ	0.00071	0.00049	0.00036	0.0001

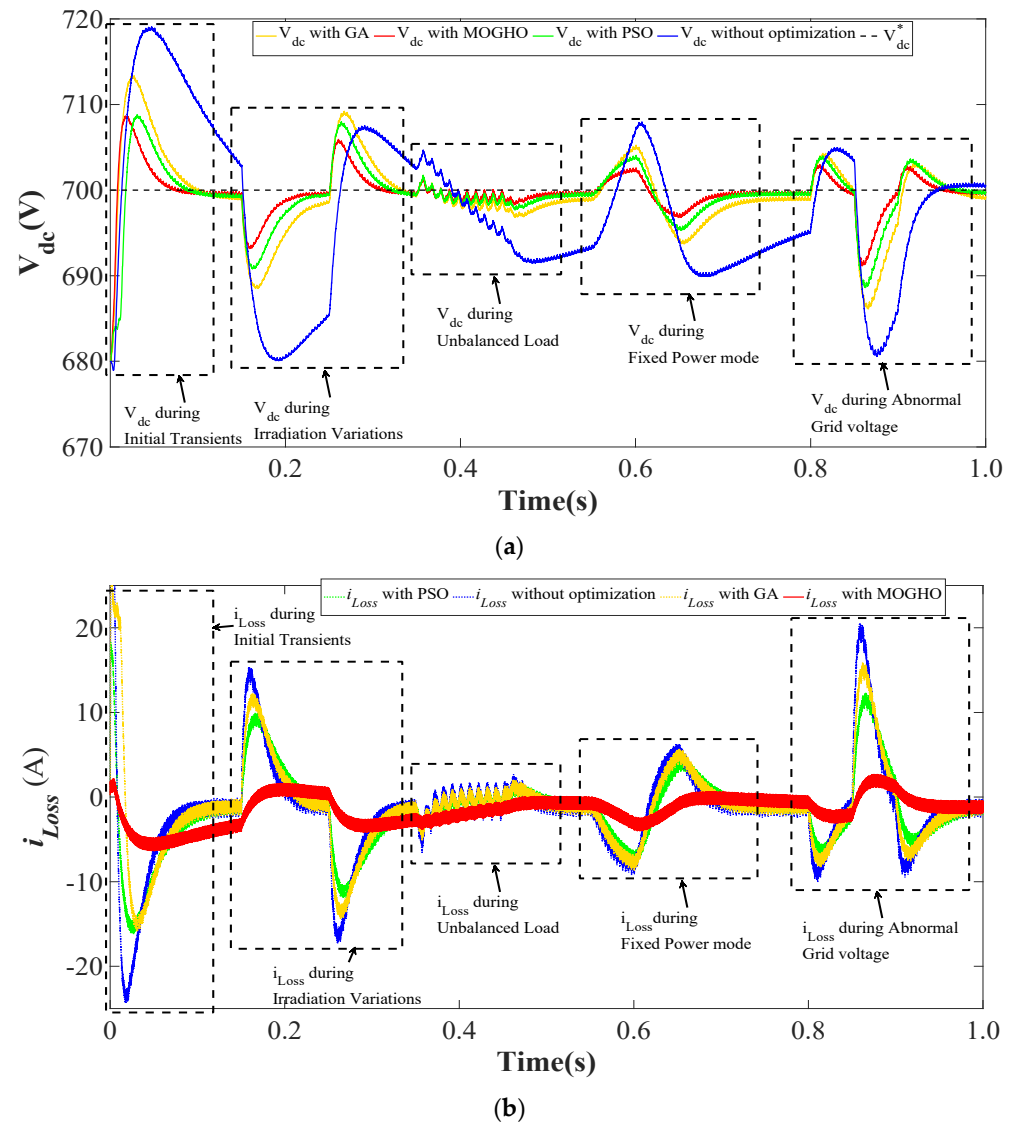


Figure 9. (a,b) Optimized V_{dc} analysis during dynamic conditions. (b) Optimized i_{Loss} current analysis during dynamic conditions system.

Table 3. Comparative performance of DC bus.

Parameters	MOGHO	PSO	GA	Without Optimization
Computational burden	High	Moderate	Moderate	None
Rise time	0.8 ms	0.85 ms	1.3 ms	1.78 ms
Settling time	3 ms	6 ms	6.5 ms	15 ms
Steady-state error	0.061%	0.064%	0.143%	0.121%
Dynamic-state error (Irradiation change)	1.800%	2.457%	2.943%	3.929%
Dynamic-state error (Load unbalancing)	0.200%	0.571%	0.671%	1.857%
Dynamic-state error (Fixed power mode)	0.829%	1.243%	1.643%	2.571%
Dynamic-state error (Abnormal grid voltage)	1.686%	2.200%	2.586%	3.486%
Transient-state error	1.229%	1.264%	1.886%	2.714%

6.3. Steady-State Analysis

The steady-state is simulated by maintaining the solar irradiation level at 1000 W/m^2 . The total harmonics distortion (THD) of phase ‘a’ of grid voltage (v_{Sa}), grid current (i_{Sa}), load voltage (v_{La}), and load current (i_{La}) are satisfactory as per IEEE519 standards are

shown in Figure 10a–d. Table 4. presents the comparative THD analysis of v_{Sa} and i_{Sa} during steady-state with MOGHO, PSO, GA and without optimization technique. With the MOGHO algorithm the proposed system delivers comparatively minimum THD.

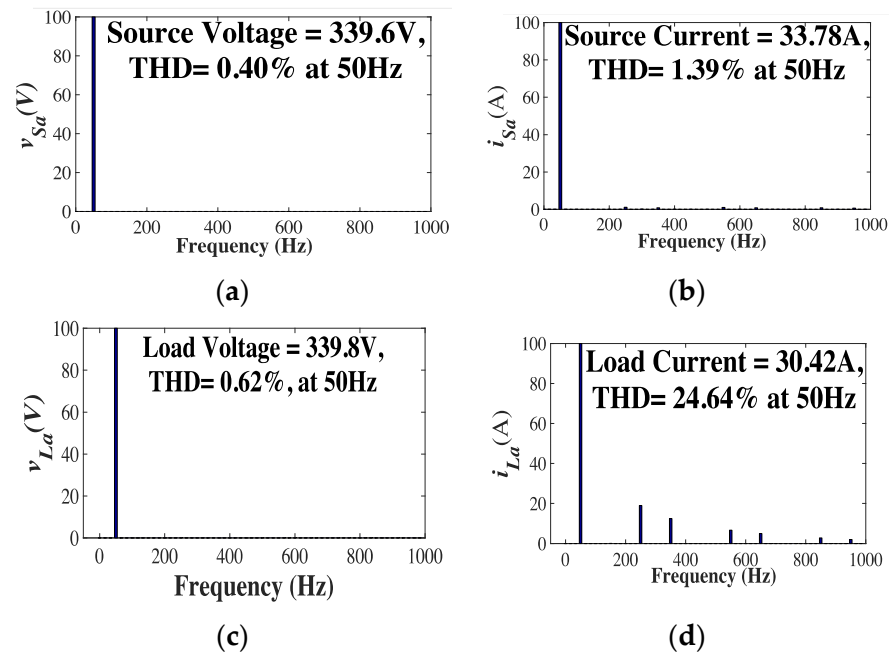


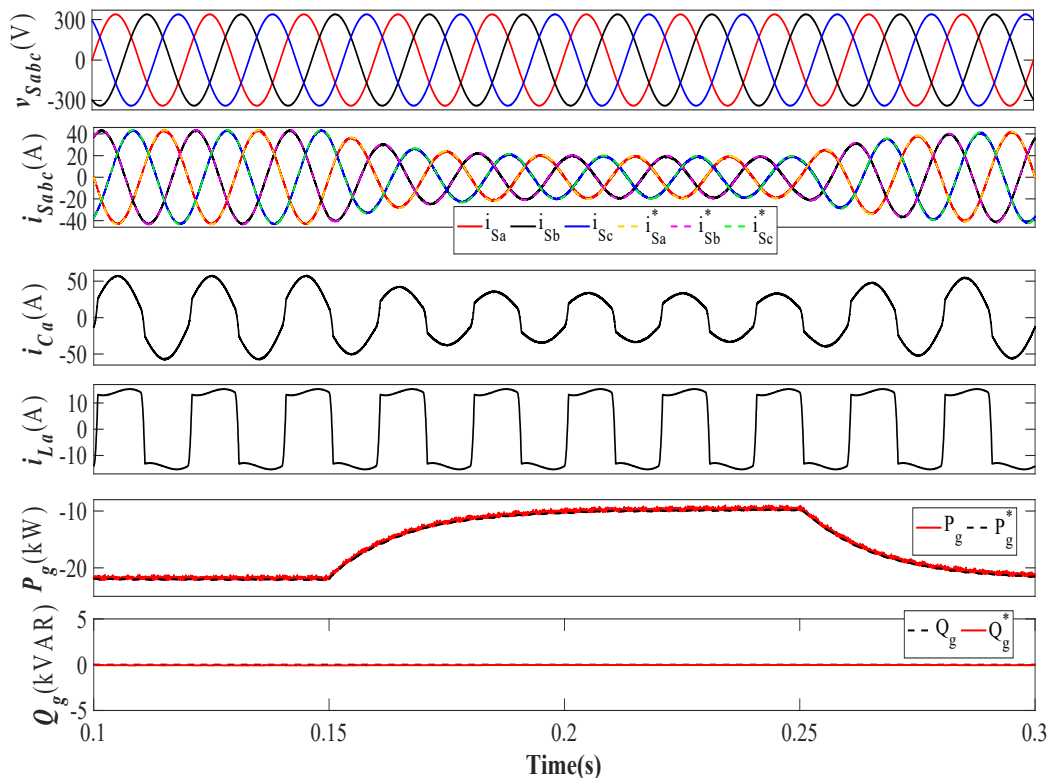
Figure 10. (a–d) THD analysis of v_{Sa} , i_{Sa} , v_{La} and i_{La} .

Table 4. THD comparison of v_{Sa} , i_{Sa} , v_{La} , i_{La} with AKWSOMCC based VSC controls.

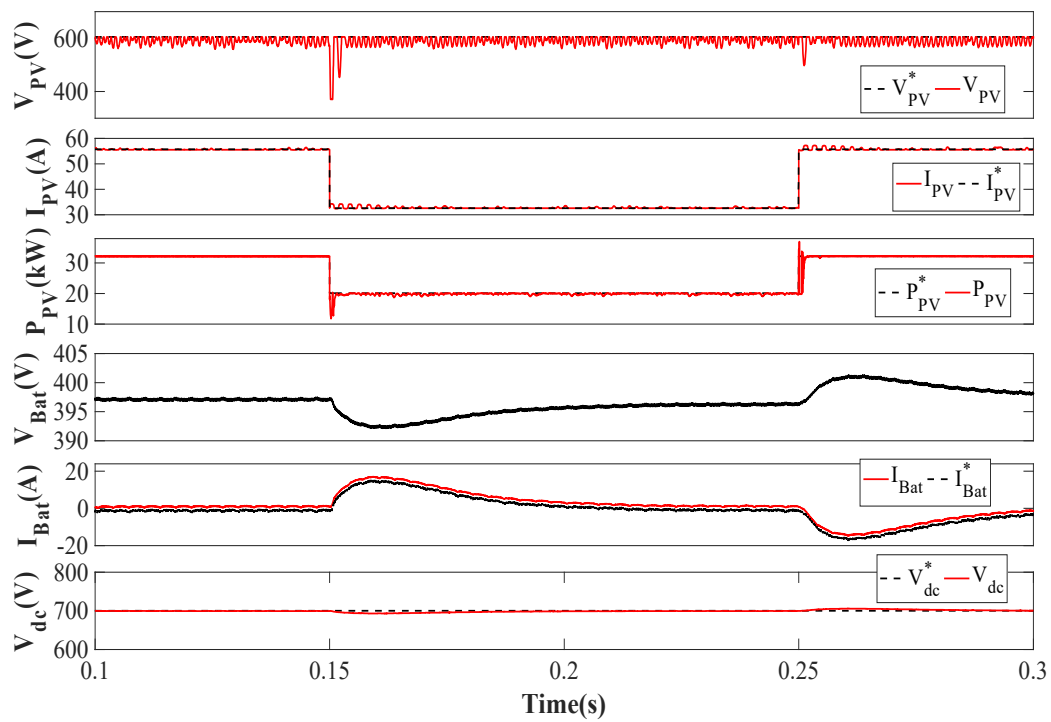
Parameters	MOGHO	PSO	GA	Without Optimization
v_{Sa}	0.40%	0.44%	0.43%	0.49%
i_{Sa}	1.39%	1.89%	2.37%	2.82%
v_{La}	0.62%	0.61%	0.62%	0.62%
i_{La}	24.64%	24.64%	24.64%	24.64%

6.4. Irradiation Variation Analysis

The insolation level is reduced from 1000 W/m^2 to 600 W/m^2 at 0.15 s of simulation time. The grid voltages and currents (v_{Sabc} and i_{Sabc}) remain in phase opposition, but the i_{Sabc} magnitude reduces with insolation level such as P_g . The i_{Sabc} follows its reference currents (i_{Sabc}^*) during the induced dynamic condition. The P_g delivered to the grid reduces, as less power is being generated by the PV system while following its reference P_g^* . The power PV power (P_{PV}) and battery collectively are sufficient enough to satisfy the load requirements. The phase ‘a’ of load current (i_{La}) and compensator current (i_{Ca}) remains in phase with each other. The Q_g must be satisfied by the VSC itself leaving the sinusoidal nature of the source intact. The Q_g follows the $Q_g^* = 0$, which is the reference reactive power exchange from the grid as shown in Figure 11a. The PV voltage (V_{PV}), current (I_{PV}) and power (P_{PV}) are also found following the reference PV voltage (V_{PV}^*), current (I_{PV}^*) and power (P_{PV}^*). The V_{PV} settles down to 600 V after some variations with a boost converter, while I_{PV} and P_{PV} change accordingly with a reduced irradiation level. The battery voltage (V_{Bat}) and current (I_{Bat}) depict the battery’s charging and discharging rate. The I_{BAT} follows its reference signal (I_{Bat}^*). The V_{dc} is maintained at the desired level of 700 V and keep matching with its reference DC link voltage (V_{dc}^*) is also shown in Figure 11b.



(a)



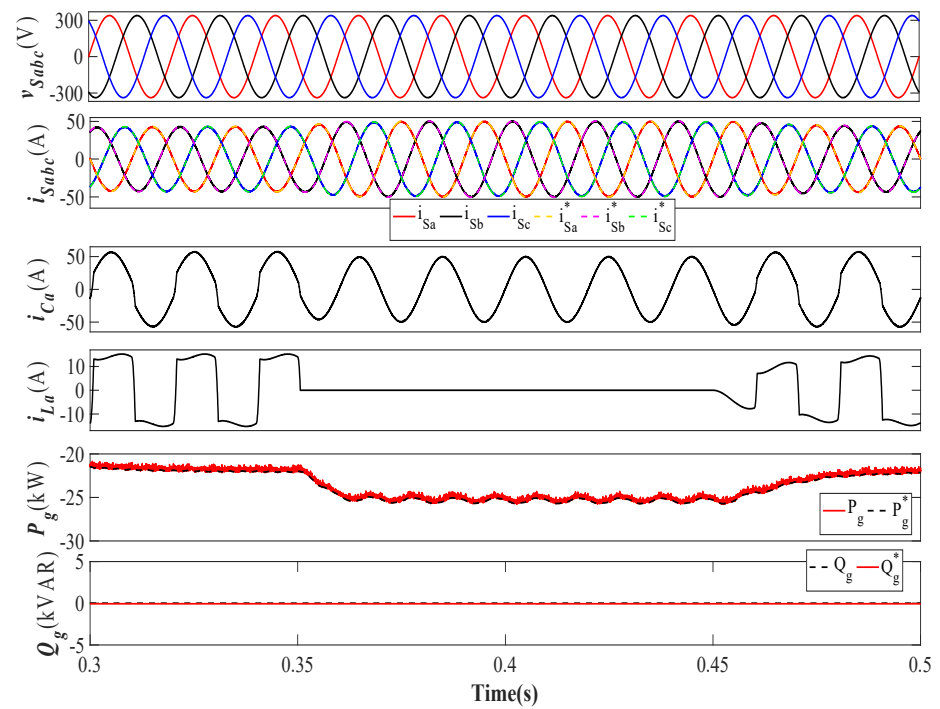
(b)

Figure 11. Irradiation variation analysis of (a) $v_{Sabc}, i_{Sabc}, i_{Ca}, i_{La}, P_g$ & Q_g (b) $V_{PV}, I_{PV}, P_{PV}, V_{Bat}, I_{Bat}$, & V_{dc} .

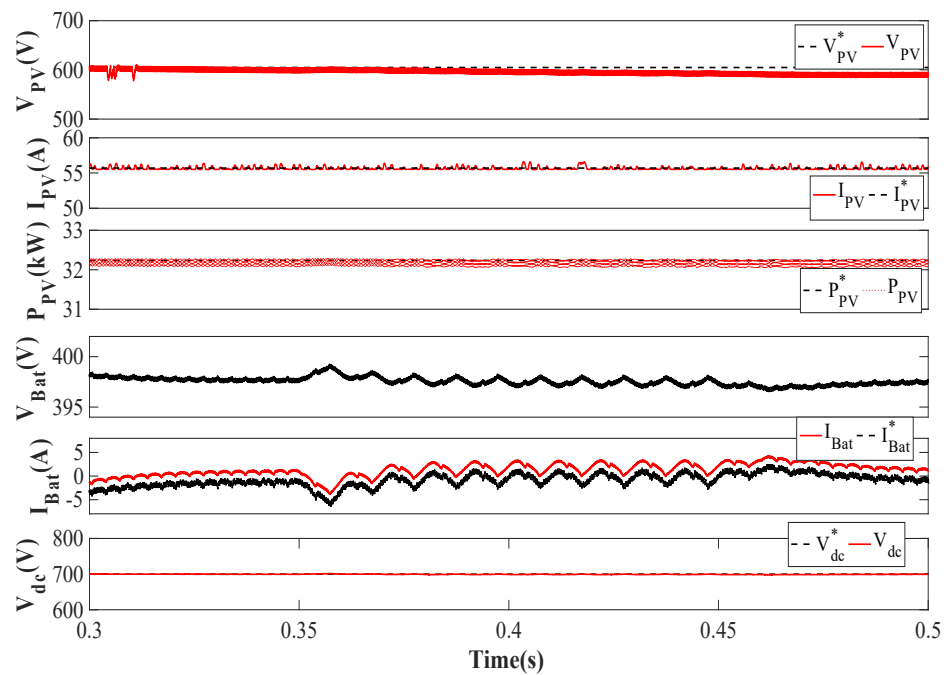
6.5. Load Unbalancing Analysis

The load unbalancing is simulated from 0.35 s to 0.45 s by removing the phase 'a' of the load. The i_{Sabc} maintains the UPF with v_{Sabc} while remaining 180° out of phase. The i_{Sabc} exactly follows i_{Sabc}^* leading towards a stable system. During load unbalancing, only two

phases of the load are connected to the system. Hence the load requirement reduces to 66% of the actual load requirement. The P_g delivered to the grid increases during unbalanced load. The Q_g exchange with grid remains zero in load unbalancing mode, as shown in Figure 12a. The V_{PV} , I_{PV} and P_{PV} remain as it is with a fixed insolation level. The I_{Bat} becomes more negative and follows I_{Bat}^* as more power is available for battery charging. The V_{Bat} also increases as the rate of battery charging increases. The V_{dc} is kept at the required level of 700 V, such as V_{dc}^* , as depicted in Figure 12b.



(a)



(b)

Figure 12. Load unbalancing analysis of (a) $v_{sabc}, i_{sabc}, i_{Ca}, i_{La}, P_g$ & Q_g (b) $V_{PV}, I_{PV}, P_{PV}, V_{Bat}, I_{Bat}$, & V_{dc} .

6.6. Specific Power Mode Analysis

The fixed or specified power mode is simulated from 0.55 s to 0.65 s of simulation time, where the system has to supply the pre-decided amount of power to the grid for handling the peak demand. The P_g varies along with i_{Sabc} as per the pre-decided grid demand. The i_{Sabc} keep following its reference signals i_{Sabc}^* while maintaining the UPF in phase opposition to v_{Sabc} . The i_{La} and i_{Ca} maintain the in-phase relation. The Q_g is also held around zero while following its reference Q_g^* as shown in Figure 13a. The V_{PV} , I_{PV} and P_{PV} shows no variation as the irradiation level is kept at 1000 W/m^2 . The I_{Bat} and V_{Bat} change according to load requirement or charging/discharging phase. The PV and battery are collectively managing the peak demand occurring on the grid. The V_{dc} is also maintained at 700 V , as V_{dc}^* , as shown in Figure 13b.

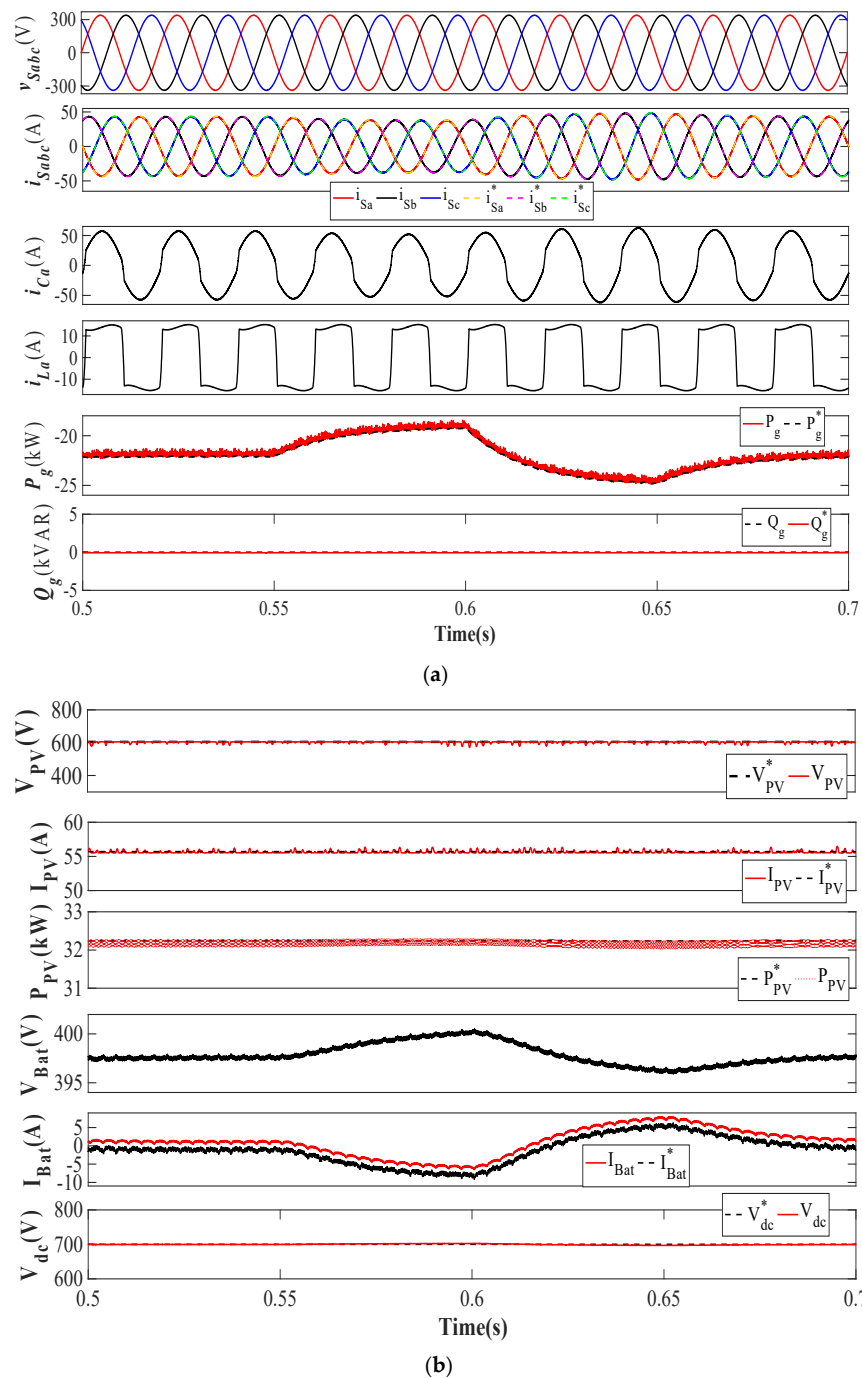


Figure 13. Specific power mode analysis of (a) $v_{Sabc}, i_{Sabc}, i_{Ca}, i_{La}, P_g$ & Q_g (b) $V_{PV}, I_{PV}, P_{PV}, V_{Bat}, I_{Bat}$, & V_{dc} .

6.7. Abnormal Grid Voltage Analysis

The grid voltage abnormality is simulated by changing the magnitude of v_{Sabc} to 0.8 p.u. and 1.2 p.u. from 0.75 s to 0.85 s of simulation time. As the v_{Sabc} changes i_{Sabc} has to change to maintain the balance of power. The i_{Ca} and i_{La} remain in phase with each other. The P_g changes abruptly with the abnormal grid voltage but settle down quickly. The Q_g exchange with the grid is kept zero as Q_g^* as shown in Figure 14a. The V_{PV} , I_{PV} and P_{PV} remain unchanged other than minor transients. The I_{Bat} changes from charging to discharging mode as the grid voltage goes through sag and swell. The V_{dc} is maintained at the desired level of 700 V as shown in Figure 14b.

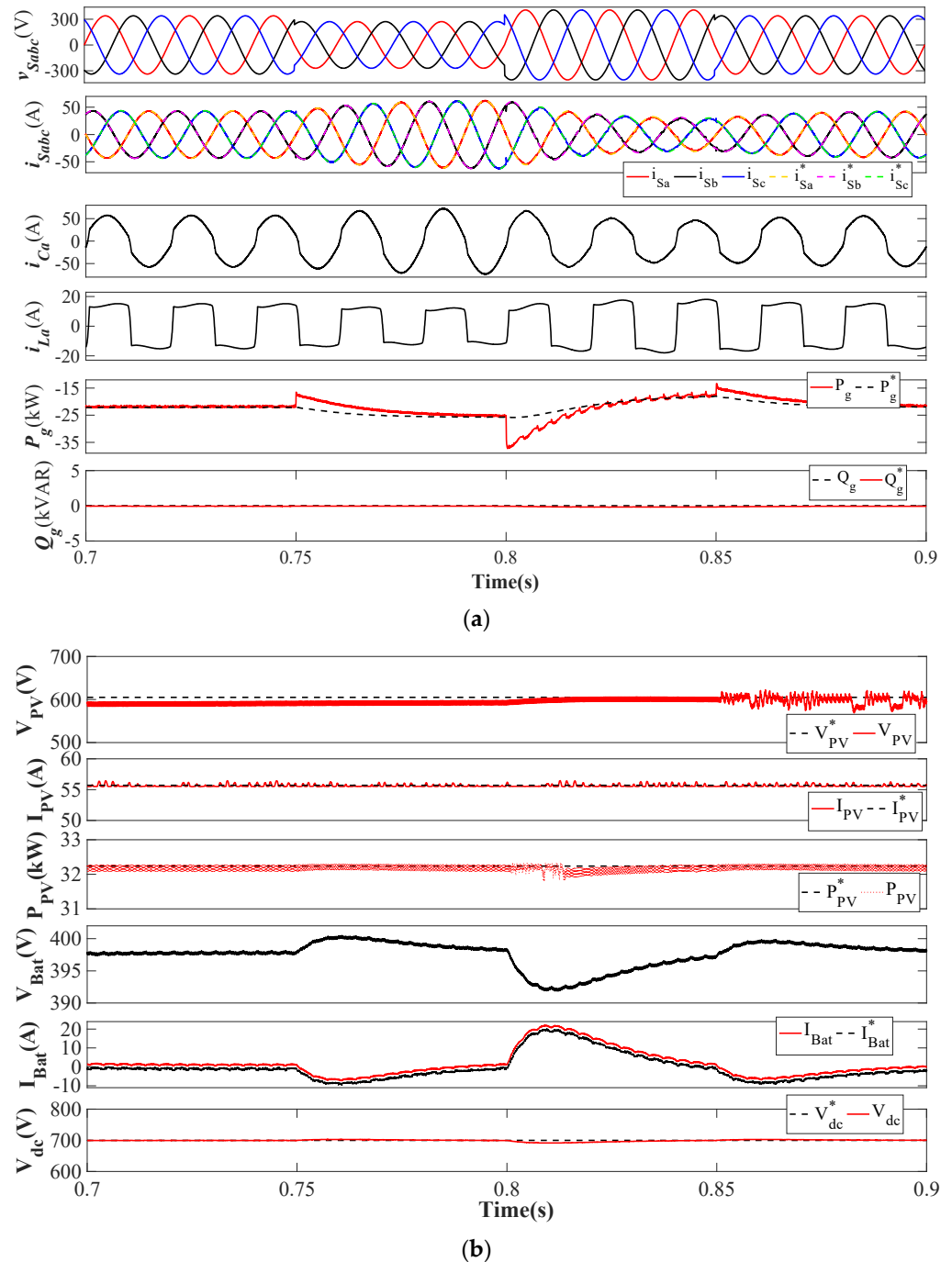


Figure 14. Abnormal grid voltage variation analysis of (a) $v_{sabc}, i_{sabc}, i_{Ca}, i_{La}, P_g$ & Q_g (b) $V_{PV}, I_{PV}, P_{PV}, V_{Bat}, I_{Bat}$, & V_{dc} .

6.8. Internal Control Signals Analysis

The internal control signals involving μ_{pa} , i_{sa}^* , W_{avg} , W_{PV} , and W_{sp} are presented in Figure 15. The μ_{pa} remains sinusoidal with unity magnitude throughout the operation. The i_{sa}^* magnitude changes under the induced diverse dynamic conditions. The W_{avg} reduces during load unbalancing, as the weight signal of phase ‘a’ diminishes to zero. The W_{avg} also varies during abnormal grid voltage as weight signals of each phase changes as per voltage sag and swell. The W_{PV} tries to balance the active power flow through the DC link. The W_{sp} varies as a function of W_{avg} and W_{PV} . Figure 16 shows the W_{avg} variations with proposed AKWSOMCC, MCC, LMF and LMS control during diverse dynamic conditions. The AKWSOMCC control delivers W_{avg} with the minimum steady-state and dynamic state error. The convergence speed of the proposed control is also comparable with LMS and LMF controls. As the W_{avg} is having reduced ripples with the proposed control, which offers better VSC performance and reduced overall losses in the system.

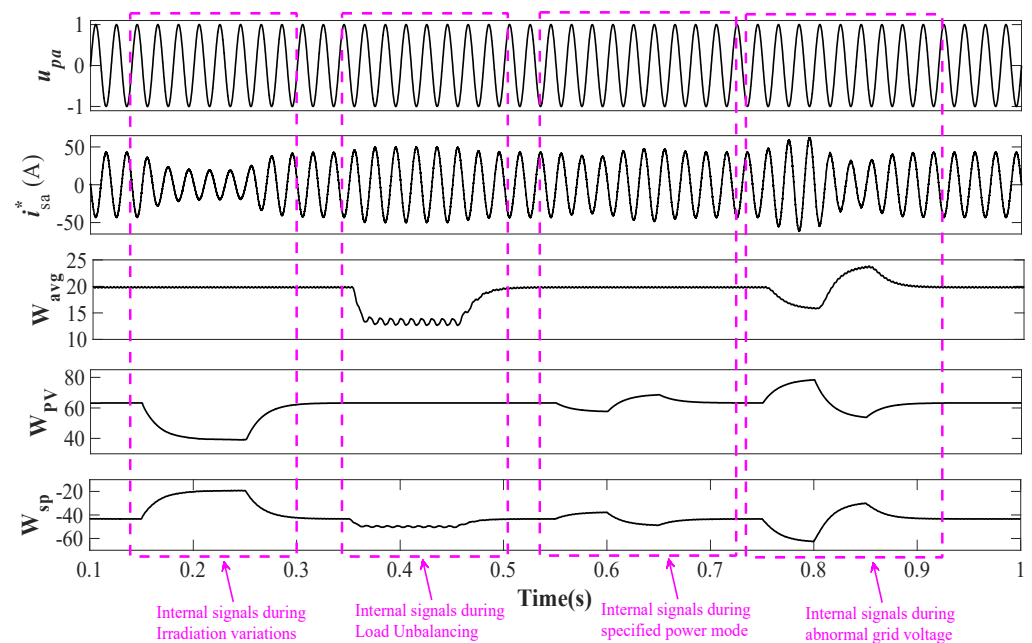


Figure 15. Internal control signal analysis of μ_{pa} , i_{sa}^* , W_{avg} , W_{PV} , and W_{sp} .

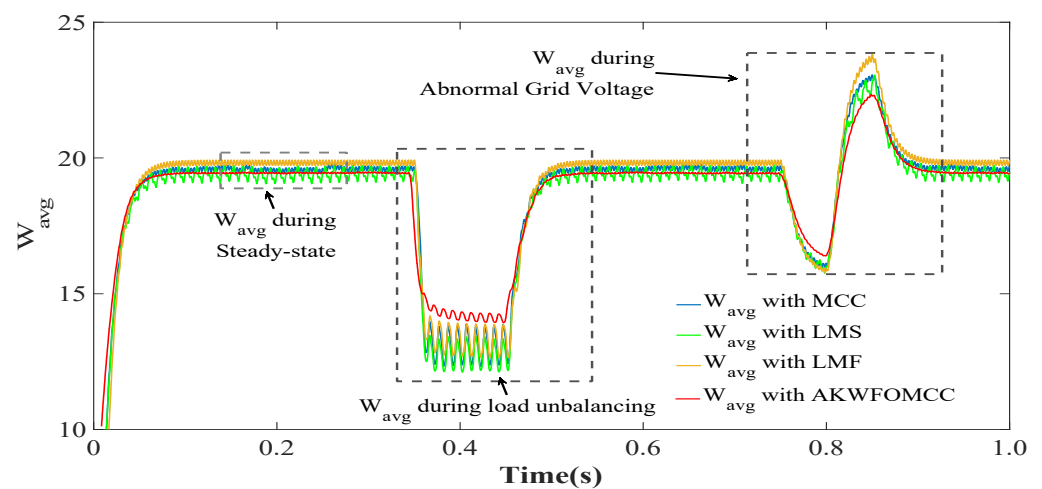


Figure 16. Average weights W_{avg} with AKWSOMCC, MCC, LMF and LMS algorithm.

7. Future Research Direction

The authors wish to extend the presented work by utilizing the optimization techniques for reducing the switching losses of the VSC and boost converter and validating it through hardware implementation.

8. Conclusions

In the 3P-3W grid-tied dual-stage PV-battery storage system, a nature-inspired meta-heuristic technique named MOGHO algorithm has been implemented for optimization of modulation factor for VSS-InC MPPT algorithm and PI controller gains for DC bus regulation. The VSS-InC with the optimized modulation factor offers faster and accurate maximum power point (MPP) tracking with reduced oscillations across MPP. With optimization implemented, the settling time of PV voltage and current have been greatly reduced from 13.2 ms to 2.1 ms just after sudden irradiation change along with oscillations. The boost converter efficiency has also swollen from 98.82% to 99.82% with optimized VSS-InC MPPT. The MOGHO tuned DC bus optimization offers enhanced system's stability during dynamic conditions and produces an accurate loss component of current. The accurate loss component of current further improves the AKWSOMCC based VSC control capability by extracting a precise fundamental component of current. The V_{dc} rise time and settling time have been lessened to 0.8 ms and 3 ms with MOGHO in comparison with PSO, GA and non-optimized DC bus. Moreover, with MOGHO the steady-state and dynamic state error of V_{dc} are obtained as low as 0.061% and 0.2% respectively. Due to the combined effect of optimized MPPT and DC bus, the VSC efficiency is grown from 98.47% to 99.23% and collective conduction losses of the boost converter and VSC have also been reduced from 875 W to 308 W. The parameter optimization is carried out on an offline basis, considering diverse dynamic conditions, to obtain the desired system's performance during online operation without slowing down the convergence speed of the system. The AKWSOMCC based VSC control, with adaptive kernel width, acts as a higher-order filter against both Gaussian and non-Gaussian noises, without affecting the convergence speed. The AKWSOMCC control performs multi-functional operations, i.e., harmonics elimination, load balancing, reactive power compensation and active power balancing during dynamic conditions. The presented system operates satisfactorily as per IEEE 519 standards.

Author Contributions: The presented work was developed by the following contributions: conceptualization, methodology: M.C. and H.M.; software, formal analysis, research, writing—original draft preparation: I.H. and A.A.; writing—review and editing, and supervising: H.M.; writing—review and editing, and supervising: F.P.G.M. All authors have read and agreed to the published version of the manuscript.

Funding: The work reported herewith has been supported by Intelligent Prognostic Private Limited, Delhi India (Project Number: XX-02), and J&K Science Technology and Innovation Council, Department of Science and Technology, Jammu & Kashmir (JKST&IC/75/2020).

Conflicts of Interest: The authors declare no conflict of interest.

Nomenclature

D	Duty cycle
ΔD	Duty cycle perturbation
δ	Scaling factor
K_p, K_i	PI controller gains
i_{Loss}	Loss component of current (A)
V_t	Voltage magnitude (V)
V_{PV}	PV voltage (V)

V_{PV}^*	Reference PV voltage (V)
I_{PV}	PV current (A)
I_{PV}^*	Reference PV current (A)
P_{PV}	PV power (kW)
P_{PV}^*	Reference PV power (kW)
V_{dc}	DC bus voltage (V)
V_{dc}^*	Reference DC bus voltage (V)
P_i	Fitness function
S_i	Social interaction term
$S(r)$	Social force
G_i	Gravity term
g	Gravitational constant
A_i	Wind advection term
\hat{e}_w	Unit vector in wind direction
\hat{e}_g	Unit vector towards earth's centre
$c = c_1 = c_2$	Comfort zone coefficient
t_{max}	Maximum iteration
r_1, r_2, r_3	Random numbers between [1, 0]
f	Attraction intensity
l	Attraction length scale
d_{ij}	Distance between i^{th} and j^{th} grasshopper
I_{Bat}	Battery current (A)
I_{Bat}^*	Reference battery current (A)
I_{Bat}^{max}	Maximum battery current (A)
V_{Bat}	Battery voltage (V)
σ_n	Adaptive kernel width
σ_0	Fixed kernel width
$e_{nx}(x = a, b, c)$	Error signals
$\mu_{px}(x = a, b, c)$	In-phase components
$W_{Px}(x = a, b, c)$	Weight signals
W_{avg}	Average weight signals
W_{PV}	Feed forward term
W_{SP}	Overall weight
$W_{SP_{fix}}$	W_{SP} during fixed power mode
v_{Sabc}	Source voltage (V)
i_{Sabc}	Source current (A)
$i_{Sx}^*(x = a, b, c)$	Reference source current (A)
$i_{Sx_{fix}}^*(x = a, b, c)$	Fixed power mode reference currents (A)
v_{Sa}	Source voltage phase 'a' (V)
i_{Sa}	Source current phase 'a' (A)
v_{La}	Load voltage phase 'a' (V)
i_{La}	Load current phase 'a' (A)
P_g	Power delivered to grid (W)
P_g^*	Reference P_g
Q_g	Reactive power delivered to grid (W)
Q_g^*	Reference Q_g
ub_j, lb_j	Upper and lower bound
N	No. of search agents
3P-3W	Three-phase three-wire
ANN	Artificial neural network
MOSHO	Multi-objective grasshopper optimization
VSC	Voltage source converter
AKWSOMCC	Adaptive kernel width sixth order maximum correntropy criteria
InC	Incremental conductance
VSS-InC	Variable step-size InC
PI	Proportional integral

ISE-1	Integral Square Error-1
ISE-2	Integral Square Error-2
Obj-1	First objective function
Obj-2	Second objective function
SI	Swarm intelligence
GA	Genetic algorithm
PSO	Particle swarm optimization
PV	Photovoltaic
P&O	Perturb and observe
VSS-P&O	Variable step-size P&O
MPPT	Maximum power point tracking
MPP	Maximum power point
MOT	Meta-heuristic optimization technique
SSO	Salp swarm optimization
GNDO	Generalized normal distribution optimization
WOA	Whale optimization algorithm
DRL	Deep reinforcement learning
SAC	Soft actor-critic
DDPG	Deep reinforcement policy gradient
EADDPG	Expert assistant DDPG
SRF	Synchronous reference frame
PBT	Power balance theory
IARC	Instantaneous active reactive control
AARC	Average active reactive control
BPSC	Balanced positive sequence compensation
PNSC	Positive negative sequence compensation
KFC	Kalman filter based controls
ST	Stockwell transformation
LMS	Least mean square
LMF	Least mean fourth
MCC	Maximum correntropy criteria
HCLMS	Hyperbolic cosine LMS
HTF	Hyperbolic tangent function
ANF-LMS	Adaptive neuro-fuzzy LMS
ZALMF	Zero attracting LMF
NMCC	Normalized MCC
FFP	Fixed forward prediction
PCC	Point of common coupling
MSE	Mean square error
THD	Total harmonics distortion

Appendix A

PV array: Kyocera GT200 module, 23 and 7 panels connected in series and parallel, $V_{pv} = 604.9$ V, $I_{pv} = 53.32$ A & $P_{pv} = 32.3$ kW; buck-boost converters parameters, $L_i = 4$ mH; boost converter parameters, $L_b = 3.11$ mH; optimized PI gains and δ :- with GA, $K_p = 0.82$, $K_i = 0.38$, $\delta = 0.00036$; with PSO, $K_p = 0.94$, $K_i = 0.71$, $\delta = 0.000049$; with MOSHO, $K_p = 1.22$, $K_i = 0.89$, $\delta = 0.00071$; initial values $K_{Pdc} = 1$, $K_{idc} = 0$ and $\delta = 0.0001$; pre-decided kernel width, $\sigma_0 = 10$; battery parameters, $V_{Bat} = 400$, $I_{Bat} = 14$ Ah, battery capacity = 5.6 kWh; MOSHO parameters, $c_{max} = 1$ and $c_{min} = 0.000001$, $t_{max} = 50$, population size = 50, lower and upper bounds for $K_p = [0, 3]$, $K_{idc} = [0, 3]$ and $\delta = [0, 0.1]$; sampling time, $T_s = 10$ μ s.

References

- Alluhaybi, K.; Member, S.; Batarseh, I. Comprehensive Review and Comparison of Microinverters. *IEEE J. Emerg. Sel. Top. Power Electron.* **2019**, *8*, 1310–1329. [[CrossRef](#)]
- Gandhi, O.; Kumar, D.S.; Rodríguez-Gallegos, C.D.; Srinivasan, D. Review of power system impacts at high PV penetration Part I: Factors limiting PV penetration. *Sol. Energy* **2020**, *210*, 181–201. [[CrossRef](#)]
- Kumar, D.S.; Gandhi, O.; Rodríguez-Gallegos, C.D.; Srinivasan, D. Review of power system impacts at high PV penetration Part II: Potential solutions and the way forward. *Sol. Energy* **2020**, *210*, 202–221. [[CrossRef](#)]

4. Mao, M.; Cui, L.; Zhang, Q.; Guo, K.; Zhou, L.; Huang, H. Classification and summarization of solar photovoltaic MPPT techniques: A review based on traditional and intelligent control strategies. *Energy Rep.* **2020**, *6*, 1312–1327. [[CrossRef](#)]
5. Karami, N.; Moubayed, N.; Outbib, R. General review and classification of different MPPT Techniques. *Renew. Sustain. Energy Rev.* **2017**, *68*, 1–18. [[CrossRef](#)]
6. Motahhir, S.; El Hammoumi, A.; El Ghzizal, A. The most used MPPT algorithms: Review and the suitable low-cost embedded board for each algorithm. *J. Clean. Prod.* **2020**, *246*, 118983. [[CrossRef](#)]
7. Messalti, S.; Harrag, A.; Loukriz, A. A new variable step size neural networks MPPT controller: Review, simulation and hardware implementation. *Renew. Sustain. Energy Rev.* **2017**, *68*, 221–233. [[CrossRef](#)]
8. Loukriz, A.; Haddadi, M.; Messalti, S. Simulation and experimental design of a new advanced variable step size Incremental Conductance MPPT algorithm for PV systems. *ISA Trans.* **2016**, *62*, 30–38. [[CrossRef](#)]
9. Mei, Q.; Shan, M.; Liu, L.; Guerrero, J.M. A novel improved variable step-size incremental-resistance MPPT method for PV systems. *IEEE Trans. Ind. Electron.* **2011**, *58*, 2427–2434. [[CrossRef](#)]
10. Bhattacharyya, S.; Kumar P, D.S.; Samanta, S.; Mishra, S. Steady output and fast tracking MPPT (SOFT-MPPT) for P&O and InC algorithms. *IEEE Trans. Sustain. Energy* **2021**, *12*, 293–302. [[CrossRef](#)]
11. Pandey, A.; Dasgupta, N.; Mukerjee, A.K. High-performance algorithms for drift avoidance and fast tracking in solar MPPT system. *IEEE Trans. Energy Convers.* **2008**, *23*, 681–689. [[CrossRef](#)]
12. Jiang, Y.; Qahouq, J.A.A.; Haskew, T.A. Adaptive step size with adaptive-perturbation-frequency digital MPPT controller for a single-sensor photovoltaic solar system. *IEEE Trans. Power Electron.* **2013**, *28*, 3195–3205. [[CrossRef](#)]
13. Chen, Y.T.; Lai, Z.H.; Liang, R.H. A novel auto-scaling variable step-size MPPT method for a PV system. *Sol. Energy* **2014**, *102*, 247–256. [[CrossRef](#)]
14. Liu, F.; Duan, S.; Liu, F.; Liu, B.; Kang, Y. A variable step size INC MPPT method for PV systems. *IEEE Trans. Ind. Electron.* **2008**, *55*, 2622–2628. [[CrossRef](#)]
15. Ahmed, J.; Salam, Z. A Modified P and O Maximum Power Point Tracking Method with Reduced Steady-State Oscillation and Improved Tracking Efficiency. *IEEE Trans. Sustain. Energy* **2016**, *7*, 1506–1515. [[CrossRef](#)]
16. Kumar, N.; Hussain, I.; Singh, B.; Panigrahi, B.K. Self-Adaptive Incremental Conductance Algorithm for Swift and Ripple-Free Maximum Power Harvesting from PV Array. *IEEE Trans. Ind. Inform.* **2018**, *14*, 2031–2041. [[CrossRef](#)]
17. Mansoor, M.; Mirza, A.F.; Ling, Q.; Javed, M.Y. Novel Grass Hopper optimization based MPPT of PV systems for complex partial shading conditions. *Sol. Energy* **2020**, *198*, 499–518. [[CrossRef](#)]
18. Jumani, T.A.; Mustafa, M.W.; Alghamdi, A.S.; Rasid, M.M.; Alamgir, A.; Awan, A.B. Swarm Intelligence-Based Optimization Techniques for Dynamic Response and Power Quality Enhancement of AC Microgrids: A Comprehensive Review. *IEEE Access* **2020**, *8*, 75986–76001. [[CrossRef](#)]
19. Mishra, S.; Ray, P.K. Power Quality Improvement Using Photovoltaic Fed DSTATCOM Based on JAYA Optimization. *IEEE Trans. Sustain. Energy* **2016**, *7*, 1672–1680. [[CrossRef](#)]
20. Chankaya, M.; Hussain, I.; Ahmad, A.; Khan, I.; Muyeen, S.M. Nyström Minimum Kernel Risk-Sensitive Loss Based Seamless Control of Grid-Tied PV-Hybrid Energy Storage System. *Energies* **2021**, *14*, 1356. [[CrossRef](#)]
21. Chankaya, M.; Hussain, I.; Ahmad, A.; Malik, H.; Márquez, F.P.G. Generalized Normal Distribution Algorithm-Based Control of 3-Phase 4-Wire Grid-Tied PV-Hybrid Energy Storage System. *Energies* **2021**, *14*, 4355. [[CrossRef](#)]
22. Mosaad, M.I.; Ramadan, H.S.M.; Aljohani, M.; El-Naggar, M.F.; Ghoneim, S.S.M. Near-Optimal PI Controllers of STATCOM for Efficient Hybrid Renewable Power System. *IEEE Access* **2021**, *9*, 34119–34130. [[CrossRef](#)]
23. Wu, J.; Wei, Z.; Li, W.; Wang, Y.; Li, Y.; Sauer, D.U. Battery Thermal-and Health-Constrained Energy Management for Hybrid Electric Bus Based on Soft Actor-Critic DRL Algorithm. *IEEE Trans. Ind. Inform.* **2021**, *17*, 3751–3761. [[CrossRef](#)]
24. Wei, Z.; Quan, Z.; Wu, J.; Li, Y.; Pou, J.; Zhong, H. Deep Deterministic Policy Gradient-DRL Enabled Multiphysics-Constrained Fast Charging of Lithium-Ion Battery. *IEEE Trans. Ind. Electron* **2021**, in press. [[CrossRef](#)]
25. Wu, J.; Wei, Z.; Liu, K.; Quan, Z.; Li, Y. Battery-Involved Energy Management for Hybrid Electric Bus Based on Expert-Assistance Deep Deterministic Policy Gradient Algorithm. *IEEE Trans. Veh. Technol.* **2020**, *69*, 12786–12796. [[CrossRef](#)]
26. Bhim, S.; Chandra, A.; Al-haddad, K. Power Quality Problems and Mitigation Techniques-Wiley Online Library. Available online: <http://onlinelibrary.wiley.com/book/10.1002/9781118922064> (accessed on 1 January 2015).
27. Abbassi, R.; Marrouchi, S.; Saidi, S.; Abbassi, A.; Chebbi, S. Optimal energy management strategy and novel control approach for DPGSs under unbalanced grid faults. *J. Circuits Syst. Comput.* **2019**, *28*, 1950057. [[CrossRef](#)]
28. Shen, M.; Xiong, K.; Wang, S. Multikernel adaptive filtering based on random features approximation. *Signal Process.* **2020**, *176*, 107712. [[CrossRef](#)]
29. Kumar, R.; Singh, B.; Kumar, R.; Marwaha, S. Recognition of underlying causes of power quality disturbances using stockwell transform. *IEEE Trans. Instrum. Meas.* **2020**, *69*, 2798–2807. [[CrossRef](#)]
30. Agarwal, R.K.; Hussain, I.; Singh, B. Application of LMS-based NN structure for power quality enhancement in a distribution network under abnormal conditions. *IEEE Trans. Neural Netw. Learn. Syst.* **2018**, *29*, 1598–1607. [[CrossRef](#)] [[PubMed](#)]
31. Agarwal, R.K.; Hussain, I.; Singh, B. LMF-based control algorithm for single stage three-phase grid integrated solar PV system. *IEEE Trans. Sustain. Energy* **2016**, *7*, 1379–1387. [[CrossRef](#)]

32. Modi, G.; Kumar, S.; Singh, B. A Maximum Correntropy Criteria Based Adaptive Algorithm for an Improved Power Quality SPV System. In Proceedings of the 8th IEEE Power India International Conference (PIICON), Kurukshetra, India, 10–12 December 2018; pp. 1–6. [[CrossRef](#)]
33. Kumar, A.; Seema; Singh, B.; Jain, R. Double stage grid-tied solar PV system using HC-LMS control. In Proceedings of the 2020-9th IEEE Power India International Conference (PIICON), Sonapat, India, 28 February–1 March 2020; pp. 3–8. [[CrossRef](#)]
34. Jain, V.; Hussain, I.; Singh, B. A HTF-Based Higher-Order Adaptive Control of Single-Stage Grid-Interfaced PV System. *IEEE Trans. Ind. Appl.* **2019**, *55*, 1873–1881. [[CrossRef](#)]
35. Srinivas, M.; Hussain, I.; Singh, B. Combined LMS–LMF-Based Control Algorithm of DSTATCOM for Power Quality Enhancement in Distribution System. *IEEE Trans. Ind. Electron.* **2016**, *63*, 4160–4168. [[CrossRef](#)]
36. Badoni, M.; Singh, A.; Singh, B. Adaptive Neurofuzzy Inference System Least-Mean-Square-Based Control Algorithm for DSTATCOM. *IEEE Trans. Ind. Inform.* **2016**, *12*, 483–492. [[CrossRef](#)]
37. Singh, A.K.; Hussain, I.; Singh, B. Double-Stage Three-Phase Grid-Integrated Solar PV System With Fast Zero Attracting Normalized Least Mean Fourth Based Adaptive Control. *IEEE Trans. Ind. Electron.* **2018**, *65*, 3921–3931. [[CrossRef](#)]
38. Chankaya, M.; Hussain, I.; Ahmad, A. Seamless control of grid-tied PV-Hybrid Energy Storage System. *Int. J. Emerg. Electr. Power Syst.* **2021**, *22*, 000010151520210090. [[CrossRef](#)]
39. Jain, V.; Hussain, I.; Singh, B. A FFP Based Adaptive Control of SPV System Tied to Weak Grid. *IEEE Trans. Ind. Appl.* **2018**, *54*, 3112–3121. [[CrossRef](#)]
40. Chankaya, M.; Ahmad, A.; Hussain, I. Adaptive Kernel Width Maximum Correntropy based VSC control of grid-tied PV-BESS System. In Proceedings of the 2021 1st International Conference on Power Electronics and Energy (ICPEE), Shillong, Meghalaya, India, 5–7 March 2021; pp. 1–6.